



## STRESS FIELD INTERACTION AND STRAIN ENERGY DISTRIBUTION BETWEEN A STATIONARY MAIN CRACK AND ITS PROCESS ZONE

ANTONIO BRENCICH and ALBERTO CARPINTERI†

Department of Structural Engineering, Politecnico di Torino, C.so Duca degli Abruzzi 24, 10129 Torino, Italy

**Abstract**—The damage process zone developed by brittle materials in front of a macrocrack is simulated by means of a distribution of microcracks. Crack mutual interactions are taken into account by means of a numerical technique, based on a displacement discontinuity boundary element method that is able of considering both the macrocrack–microcrack and microcrack–microcrack interactions inside the process zone. In the frame of linear elastic fracture mechanics the stress field at each crack tip and the related elastic strain energy are calculated. The main features of the interaction phenomena turn out to be almost independent of the microcrack density. Some considerations both on the shielding and amplification effects on the main crack and on the strain energy distribution between cracks give explanation to experimental evidence and prove that crack interaction is not such a short-range effect as sometimes expected. © 1998 Elsevier Science Ltd. All rights reserved

**Keywords**—crack interaction, energy distribution, microcrack toughening, process zone.

### NOMENCLATURE

$\alpha$	constant, set equal to 0.01
$\delta$	horizontal distance of the centre of a reference microcrack from the main crack tip
$\phi$	general orientation in the plane
$\phi_0$	orientation in which the maximum value for $\sigma_n$ is to be found
$\Delta\phi$	amplitude of the variation range for $\phi$ around the value $\phi_0$
$\nu$	Poisson coefficient
$r, \theta$	polar coordinates centred at the main crack tip
$\rho_A$	surface crack density
$\rho_V$	volume crack density
$\rho_A^{\text{sat}}$	maximum (saturated) surface crack density
$\rho_V^{\text{sat}}$	maximum (saturated) volume crack density
$\sigma_n$	stress component normal to the $\phi$ direction
$\sigma_n^{\text{max}}$	maximum value for $\sigma_n$
$\sigma_n^{\text{min}}$	minimum value for $\sigma_n$
$\sigma_n^{\text{lim}}$	reference limit stress for $\sigma_n$
$\sigma_r, \tau_{r\theta}$	polar stress components
$\mathcal{G}$	energy release rate
$A$	reference area
$G$	elastic shear modulus
$h$	vertical distance between crack centres
$H_{\text{dam}}$	vertical maximum dimension of the non saturated process zone
$H_{\text{sat}}$	vertical maximum dimension of the saturated process zone
$H_{0.4}$	vertical dimension of the limit for 40% of the saturated crack density
$K_I$	mode I stress intensity factor
$K_{II}$	mode II stress intensity factor
$K_{I0}$	mode I stress intensity factor in absence of microcracks
$K_{IC}$	material fracture toughness
$l_i$	$i$ -th crack length
$l$	average crack length
$n_{\text{mc}}$	total number of microcracks
$N_A$	number of cracks in the reference area $A$
$N_V$	number of cracks in the reference volume $V$
$r_{\text{dam}}$	maximum distance from the main crack tip of the external boundary of the non saturated process zone (in polar coordinates)
$r_{\text{sat}}$	maximum distance from the main crack tip of the external boundary of the saturated process zone (in polar coordinates)
$R_{\text{dam}}$	horizontal maximum dimension of the non saturated process zone

†Author to whom correspondence should be addressed.

$R_{\text{sat}}$	horizontal maximum dimension of the saturated process zone
$R^*$	specific value corresponding to a tangent $\alpha$ to the singular stress field
$R_I^*$	specific value of the radius $r$ for which the symmetric stress field has a value for the trigonometric tangent $\leq \alpha$
$R_{II}^*$	specific value of the radius $r$ for which the anti-symmetric stress field has a value for the trigonometric tangent $\leq \alpha$
$S_0$	horizontal distance between crack centres
$V$	reference volume
$W$	elastic strain energy density
$W_{R^*}$	elastic strain energy density contained in a circular area of radius $R^*$ centred in the main crack tip
$W_{R^*}^I$	mode I component of $W_{R^*}$
$W_{R^*}^{II}$	mode II component of $W_{R^*}$
$W_{R^*}^T$	total elastic strain energy content
$W_{R^*}^{\text{MC}}$	elastic strain energy content related to the main crack
$W_{R^*}^{\text{mc}}$	elastic strain energy content related to a microcrack
$x, y$	Cartesian coordinates centred at the main crack tip
$\langle \cdot \rangle$	average value
$\partial$	derivative.

## 1. INTRODUCTION

SOME CLASSES of brittle materials, such as ceramics and rocks, are experimentally found to undergo extensive microcracking in a limited area, located just in front and around the tip of a macroscopic crack, known as process zone [1, 2].

Microcracks originating at grain facets by local concentrations of tensile stress [1] due to thermal mismatches during manufacturing cooling processes and phase transformation in multi-phase ceramic alloys are characterized by a random distribution of orientation, length and locations inside the damaged material [3]. On the other hand, when microcracks nucleate as a consequence of the external applied loads, their geometric settlement resembles the principal stress directions but for some deviations due to material inhomogeneities.

As a macroscopic result of profuse microcracking, the propagation of the macrocrack is postponed [2, 4] and an apparent increase of the material toughness can be postulated. At a micromechanical level two different potential contributions of microcracking can be distinguished: when microcracks are nucleated the singular stress field is relieved by stress redistribution and energy dissipative mechanisms [5]; from this point on and until the macroscopic crack propagates and new microcracks are generated, the effects of the process zone on the main crack is due to the elastic interaction between cracks [6]. These two mechanisms, altogether, give origin to a shielding effect of the main crack tip which is addressed as *toughening by microcracks*.

The analytical approach to microcrack toughening can follow two different schemes. A continuum damage model looks at the microcrack cloud through some homogenizing technique suitable to obtain the stress-strain response of the damaged material. The effects of microcracking are therefore considered on the average, so that the process zone can be modelled as an area where the material exhibits degraded elastic constants [7–11]. From this point of view the cracked area is identified via some characteristic quantities such as the average microcrack density and orientation and by the geometric shape of the process zone.

A discrete approach, like the one which is followed in this work, makes use of geometrical criteria, formulated on the basis of physical grounds, to simulate the process zone by means of a distribution of microcracks. The approach, similar to that proposed by Kachanov *et al.* [12] turns out to be kinematic in the sense that the microcrack geometry is first set and then its effect on the main crack is computed. The attention is focused on a specific moment of the macrocrack history: once the process zone has been generated and the residual stresses have been relieved, further stress redistribution occurs directly from the interaction of the main crack with the microcracks and of the microcracks between themselves, which turns out to be a crucial phenomenon for the onset of propagation of the stationary main crack.

A ceramic alloy or a rock type material can be thought of as exhibiting an hyper-elastic perfectly brittle behaviour, so that a linear elastic fracture mechanics approach, describing the near-tip stress field by means of the SIFs only, is admissible. The crack arrangement is analysed under plane strain conditions, considering the matrix to be homogeneous, isotropic, with an elastic perfectly-brittle behaviour and with infinite extension. The remotely applied loads consist

of uniform traction at infinity so as to load the macrocrack in pure mode I. In this way the model is highly idealized, but nevertheless it isolates one of the essential mechanisms of microcrack toughening and its effect on shielding the main crack.

The essential features of the interaction between cracks had been studied with regard to simple geometries involving few microcracks, or, at least, periodic arrays of microcracks[13–18]. Even though the elementary mechanisms of the phenomenon had been pointed out, nevertheless only large and complex microcrack distributions can be considered as satisfactory simulations of the process zone. The complexity of these cases and the intrinsic difficulty in their analytical formulation have made it unavoidable to use numerical tools[16, 19, 20, 21].

In this work, the main crack–microcracks interaction is taken into consideration by simulating the process zone with up to 70 cracks, both oriented perpendicular to the maximum tensile stress direction and parallel to the main crack line. The elastic problem related to the solid is solved by a numerical procedure based on displacement discontinuity boundary elements proposed by the authors[19] which proved to be highly efficient in fracture mechanics problems and allows to take into account not only the main crack–microcrack, but also the microcrack–microcrack interactions. The overall effect on the main crack is addressed via the variation of the SIF at the main crack tip with respect to the SIF which would be expected for the virgin material (absence of microcracks). The standard approach to interaction problems through discrete models[12, 14, 15, 19, 20, 22] is aimed at computing the overall effect on the main crack tip, but in this way information about the microcracks is lost.

The elastic strain energy density related to the singular stress field at a crack tip can be obtained by integrating the strain energy density function proposed by Sih[23, 24] over the area around the tip in which the singular field can be considered prevailing on the remotely applied uniform stress field, so that a general description of the interactive phenomena can be given taking into account the contribution of the microcracks to the total elastic strain energy. This aspect of the work follows the approach proposed by Shum and Hutchinson[25] from the point of view of a continuum damage model. In this way, some considerations can be deduced on the mechanics of crack interaction with its process zone, with regard also to energy exchanges between cracks.

## 2. MICROCRACK DENSITY

An estimate of the material damage can be given in terms of microcrack density. Let us consider a cracked solid containing penny-shaped cracks and a plane cross-section on which discrete traces of the cracks can be detected. Following Bristow [26], Walsh [27, 28] and Kachanov[29], the crack density parameter  $\rho$  can be defined as:

$$\rho_A = \frac{1}{A} \sum_i l_{(i)}^2, \quad (1a)$$

$$\rho_V = \frac{1}{V} \sum_i l_{(i)}^3, \quad (1b)$$

where  $l_{(i)}$  stands for the length of the  $i$ -th microcrack trace contained in the representative area  $A$  or volume  $V$ . When referring to the average length  $\langle l \rangle$ , eqs 1(a–b) are expressed by means of the number  $N_A$  of microcracks contained in the area  $A$  (or the number  $N_V$  of cracks detected in the volume  $V$ ):

$$\rho_A = \frac{1}{A} N_A \langle l \rangle^2, \quad (2a)$$

$$\rho_V = \frac{1}{V} N_V \langle l \rangle^3. \quad (2b)$$

Other definitions, such as the one given for non-circular cracks by Budiansky and O'Connell[30], differ from eqs 2(a–b) for some inessential coefficients.

The non-dimensional quantities of eqs 2(a–b) are not independent of each other since the plane cross-section image is a bi-dimensional representation of the three-dimensional distri-

Table 1. Microcrack saturated densities for different materials

Material	$\rho_V^{\text{sat}}$	$\rho_A^{\text{sat}}$	Reference
Westerly granite	—	[0.13; 0.16]	Hadley[32]
Coconino sandstone	—	[0.04; 0.06]	Gawad <i>et al.</i> [33]
Alumina–zirconia	[0.00; 0.15]	[0.00; 0.24] eq. (4)	Rühle <i>et al.</i> [3]
Silicon–carbide alloy	[0.20; 0.30]	[0.31; 0.47] eq. (4)	Han and Suresh[2]
Concrete	[0.04; 0.13]	[0.06; 0.20] eq. (4)	Nemati[34] Nemati and Monteiro[35]

bution of cracks. The number of cracks per unit volume  $N_V/V$  can then be related to the number of cracks per unit area  $N_A/A$  and the microcrack average length  $\langle l \rangle$  by the relationship[31]:

$$\frac{N_V}{V} = \frac{2 N_A}{\pi A} \frac{1}{\langle l \rangle}. \tag{3}$$

Substituting eq. (3) into eq. (2a), the following expression is obtained:

$$\rho_A = \frac{\pi}{2} \rho_V. \tag{4}$$

Table 1 summarizes the estimates for the maximum microcrack density deduced from experimental observations on brittle materials.

Reducing the three-dimensional problem to a plane one and referring to the microcrack grid represented in Fig. 1 where all the microcracks have the same length  $2l$ , the average crack density  $\rho_A$  is found to be a function of the normalized horizontal,  $S_0/l$ , and vertical,  $h/l$ , spacings between the microcrack centres:

$$\rho_A = \frac{4}{h \left( \frac{S_0}{l} + 2 \right)}. \tag{5}$$

In the case when  $S_0/l = 2h/l$ , which is a realistic choice, eq. (5) allows the definition of the geometric distribution of cracks once the microcrack density is imposed according to eq. (4) and the microcrack length  $l$  is given.

### 3. THE PROCESS ZONE

Let us consider a semi-infinite main crack loaded in pure mode I by a uniform traction  $\sigma$  at infinity. Referring to polar coordinates centred in the crack tip, in a generic point  $Q(r, \theta)$  the stress component normal to the direction defined by the angle  $\phi$ , Fig. 2, is a function of the SIF  $K_I$ :

$$\sigma_n = \frac{K_I}{\sqrt{2\pi r}} \left[ \cos \frac{\theta}{2} + \frac{1}{2} \sin \left( \frac{3}{2}\theta - 2\phi \right) \right]. \tag{6}$$

Equation (6) attains a maximum for  $\phi = (3/4)\theta - (\pi/4)$  and a minimum for  $\phi = \pm \pi/2$ , leading to the following values:

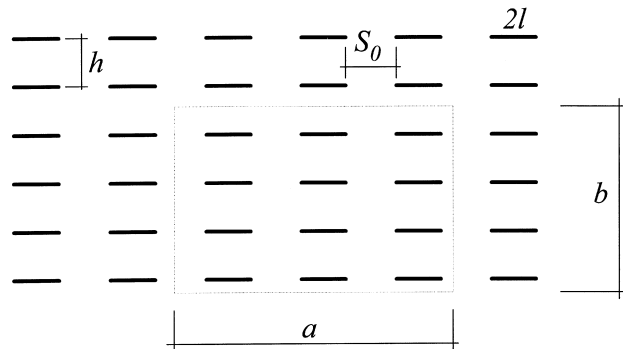


Fig. 1. Microcrack grid and spacings between crack centres.

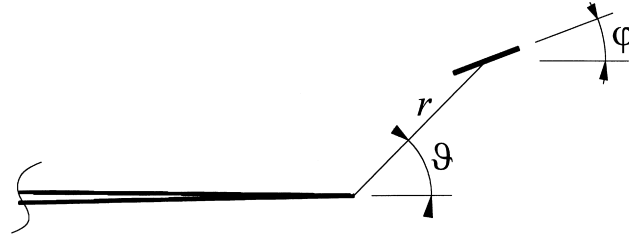


Fig. 2. Microcrack in front of the main crack tip and related quantities.

$$\sigma_n^{\max} = \frac{K_I}{\sqrt{2\pi r}} \left[ \cos \frac{\theta}{2} + \frac{1}{2} \sin \theta \right], \quad (7)$$

$$\sigma_n^{\min} = \frac{K_I}{\sqrt{2\pi r}} \left[ \cos \frac{\theta}{2} - \frac{1}{2} \sin \theta \right]. \quad (8)$$

According to Hoagland and Embury [36], Gong and Meguid [37] and Gong [22] let us assume that nucleation of a microcrack takes place when the stress component  $\sigma_n$  is higher than or equal to a limit stress  $\sigma_n^{\lim}$ , which can be considered, up to this point, a quantity related to the tensile strength of the material and to its internal microstructure:

$$\sigma_n \geq \sigma_n^{\lim}. \quad (9)$$

The maximum microcrack density is to be found in that area where the nucleation condition of eq. (9) is attained for every orientation  $\phi$  or, in other words, when:

$$\sigma_n^{\min} \geq \sigma_n^{\lim}. \quad (10)$$

When eq. (10) is satisfied the microcrack density is maximum and is called the *saturated density*. The outer boundary of this area can be obtained imposing the limit condition  $\sigma_n^{\max} = \sigma_n^{\lim}$ , in eq. (8) and solving it for the radius  $r$ :

$$r_{\text{sat}}(\theta) = \left( \frac{K_I}{\sigma_n^{\lim}} \right)^2 \frac{1}{2\pi} \left( \cos \frac{\theta}{2} - \frac{1}{2} \sin \theta \right)^2. \quad (11)$$

Similarly, the material remains undamaged when neither an orientation  $\phi$  satisfies the nucleation eq. (9); the intact material is therefore characterized by the following inequality:

$$\sigma_n^{\max} \leq \sigma_n^{\lim}. \quad (12)$$

The condition that the maximum normal traction expressed by eq. (7) equals the limit resistance,  $\sigma_n^{\max} = \sigma_n^{\lim}$ , gives the position of the most distant locations from the main crack tip at which microcracks can nucleate, which is to say the external boundary of the process zone, i.e. the limit of the damaged material:

$$r_{\text{dam}}(\theta) = \left( \frac{K_I}{\sigma_n^{\lim}} \right)^2 \frac{1}{2\pi} \left( \cos \frac{\theta}{2} + \frac{1}{2} \sin \theta \right)^2. \quad (13)$$

Equations (11) and (13) are represented in Fig. 3.

The half height  $H_{\text{sat}}$  of the saturated area is the maximum vertical component of the radius  $r_{\text{sat}}(\theta)$  which is attained for  $\theta = 31.8^\circ$ , while the maximum length  $R_{\text{sat}}$  coincides with the radius  $r$  when  $\theta$  is set to zero:

$$H_{\text{sat}} = 0.0407 \left( \frac{K_I}{\sigma_n^{\lim}} \right)^2, \quad (14a)$$

$$R_{\text{sat}} = 0.1592 \left( \frac{K_I}{\sigma_n^{\lim}} \right)^2. \quad (14b)$$

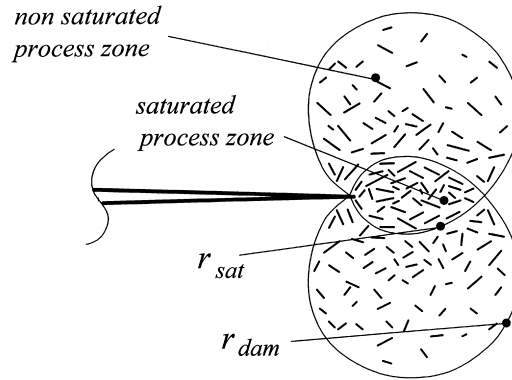


Fig. 3. Saturated microcrack density in the inner part of the process zone and external boundary of the damaged material.

In the same way, the half height of the entire process zone is given by eq. (13) for  $\theta = 74.8^\circ$ :

$$H_{\text{dam}} = 0.2505 \left( \frac{K_I}{\sigma_n^{\text{lim}}} \right)^2. \quad (15)$$

The comparison between eqs (11) and (13) shows that the length of the process zone on the crack line is the same as in eq. (14b). The area outside the saturated zone  $r > r_{\text{sat}}(\theta)$  and inside the external limit of the process zone  $r < r_{\text{dam}}(\theta)$  is characterized by a varying microcrack density. Let us suppose that in a certain point  $Q$  the nucleation eq. (9) is attained for all the orientations included in the range  $[\phi_0 - \Delta\phi, \phi_0 + \Delta\phi]$ ,  $\phi_0$  being the orientation for which the normal stress  $\sigma_n$  is maximum. Since the normal stress equals the limit stress  $\sigma_n^{\text{lim}}$  at the extremes of the range, from eq. (6) the value of the range width can be found:

$$2\Delta\phi = \cos^{-1} \left[ \frac{\sqrt{8\pi r} \sigma_n^{\text{lim}}}{\sin \theta K_I} - \frac{1}{\sin \frac{\theta}{2}} \right]. \quad (16)$$

In the generic point  $Q(r, \theta)$ , the density is finally posed as:

$$\rho_A = \frac{2\Delta\phi}{\pi} \rho_A^{\text{sat}}, \quad (17)$$

and substituting  $\theta = \pi/2$  in eqs (16) and (17), we can obtain the crack density as a function of the vertical distance  $y$  from the main crack tip:

$$\rho_A = \frac{\rho_A^{\text{sat}}}{\pi} \cos^{-1} \left[ \frac{\sigma_n^{\text{lim}}}{K_I} \sqrt{8\pi y} - \sqrt{2} \right]. \quad (18)$$

It is an open question whether the interaction phenomena with the main crack involve only the nearest microcracks, as suggested in Refs [8, 25], or also the more distant microcracks contribute to the main crack tip SIFs. In Refs [19, 38], the authors demonstrated that, according to experimental observations [2], the crack array that produces noteworthy effects on the main crack stress field is quite large when microcrack–microcrack interactions are taken into account. The simulations involving large microcrack arrays showed that very far located cracks contribute to the overall effect on the main crack for less than 3–4% since their effect is shadowed by the cracks located in the inner part of the array.

Consequently, we will assume that the microcracks located in the area where:

$$\rho_A \leq 0.4 \rho_A^{\text{sat}}, \quad (19)$$

can be neglected. The results of the simulations carried out in this work and which will be discussed later on, give further reasons for such an approximation.

Imposing eq. (19) into eq. (18) the half height of the considered area is obtained:

$$H_{0,4} = 0.1182 \left( \frac{K_I}{\sigma_n^{\text{lim}}} \right)^2, \quad (20)$$

which corresponds to an angle  $\theta = 43.9^\circ$  in eqs (16) and (17). Once the ratio  $K_I \sigma_n^{\text{lim}}$  is known, the geometric shape of the process zone is completely defined.

#### 4. SIMULATION OF THE PROCESS ZONE

The so-called *wake region* consists of the area which lies behind the process zone and is located on the two sides of the macrocrack body.

When a macrocrack grows, new microcracks are continuously generated in front of its tip so that the process zone follows the crack path; in this way previously generated microcracks are left in the wake. In the case of a stationary crack instead, such as the one which is dealt with in this work, microcracks in the wake area, if present, are the result of pre-existing microcracking. In the latter case there is much evidence that the interaction of those cracks with the main crack tip rapidly vanishes as the cracks are left behind the macrocrack tip [6, 14, 16, 18, 19, 22, 39]. This fact can be explained by noting that the wake zone is shadowed by the main crack body and the stress-free condition, which is rigorous on the crack faces, remains a reasonable approximation in the entire wake area. Calculations carried out on few microcracks, as well as on large microcrack arrays, show that when the microcrack centre enters the wake area for approximately the crack length or more, the singular stress field at its tips vanishes (the SIFs are approximately zero). The displacement discontinuity normal to the crack faces is recovered and, in a frictionless material coherent with the perfectly-elastic model herein proposed, so does the tangential displacement discontinuity. In addition, the results discussed in the following sections, which also considers the case of microcracks located in the wake area, give further evidence to this theory.

The simulation of the process zone by means of a distribution of microcracks needs the definition of a microcrack to be established. While a macrocrack can easily be defined as a crack which can be detected at a macroscopic scale, a microcrack can be addressed with different definitions. It could be considered as a crack with a length of at least one order of magnitude shorter than the macroscopic crack length, but this definition is not applicable when the main crack is thought of as semi-infinite.

On the other hand, the characteristic length of a microcrack could be related to the material microstructure, which leads to different definitions according to the observation scale adopted when describing the microstructure itself.

A reasonable hypothesis leads to the definition of the limit stress  $\sigma_n^{\text{lim}}$  as the tensile strength of the material so that this parameter, along with the fracture toughness  $K_{IC}$ , can be assumed as a macroscopic parameter for the internal microstructure and related to the microcrack characteristic length. From dimensional analysis the ratio  $K_I / \sigma_n^{\text{lim}}$  is found to have the dimension of a square rooted length; the average microcrack length  $\langle l \rangle$  can be assumed to be a fraction (for example one sixteenth) of the process zone extension  $R_{\text{sat}}$ :

$$\langle l \rangle = \frac{R_{\text{sat}}}{16} \cong \frac{0.16}{16} \left( \frac{K_{IC}}{\sigma_n^{\text{lim}}} \right)^2 \cong 0.01 \left( \frac{K_{IC}}{\sigma_n^{\text{lim}}} \right)^2. \quad (21)$$

Once the saturated density is given according to eq. (4) and the microcrack length is assumed as eq. (21), the crack spacings are obtained by means of eq. (5).

The geometric distribution of microcracks is of primary importance for every discrete model. Hoagland and Embury [36] first introduced the concept of *crack precursor* as a location where a crack can nucleate if a critical condition of the type of eq. (9) is reached on some orientation  $\phi$ . The random microstructure of a ceramic alloy, where the grains are approximately of the same size, makes it reasonable to think the *crack precursors* as regularly distributed inside the process zone and the microcracks of approximately constant length [22].

Through an evolutive analysis of microcrack nucleation in front of a stationary crack, Hoagland and Embury [36] demonstrate that the crack precursors, where cracks are generated,

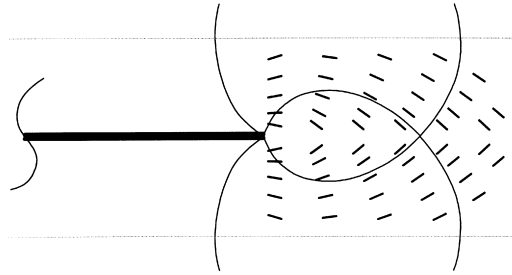


Fig. 4. Size and position of the microcrack distribution.

are distributed in an area which is approximately as wide as the prevision made on the stress field prevailing prior to microcracking, but some 40–50% longer. For this reason the microcrack distribution employed in the following analyses covers an area which is longer than the calculated process zone length, Fig. 4.

Once the microcrack average length is given according to eq. (21) and the horizontal and vertical distances between cracks is computed from eq. (4) on the basis of experimental grounds, the internal geometric shape of the process zone is defined. What still has to be discussed is the position of the first microcrack of the distribution. Given the vertical distance  $h$  from the main crack, eq. (4), the nearest crack is placed with its centre on the limit of the saturated microcracked area, Fig. 5.

Following Ref. [36], all the other microcracks are distributed so as to obtain a regular grid, but for the geometric variations due to the crack density reductions in outer areas. This choice cannot be considered as the relative position in which the microcracks are first nucleated and in fact it is not. Due to many sources of uncertainty, any criterion that can be formulated can be considered heuristic to a certain extent. For this reason the computations had been carried out for different positions of the main crack tip identified by the parameter  $\delta$  in Fig. 5. Negative values for  $\delta$  represent a process zone which is ahead of the main crack tip, while positive values mean that the macrocrack is located in a deeper position inside the microcracked area than the one represented in Fig. 4. Large negative and positive values of  $\delta$  had been considered for the sake of completeness.

Varying the parameter  $\delta$ , a series of analyses has been carried out all considering the main crack in stationary conditions. In this way, the positions of the main crack corresponding to the maximum shielding effect can be detected, positions which characterize the geometries in which microcracking toughening phenomena are expected.

For the microcrack orientations, two choices have been investigated: an orientation normal to the principal tensile stress direction and another one where all the cracks are parallel to the main one. Figure 6 represents the microcrack distributions obtained for different values of the saturated density and for both the orientations; all the figures are obtained for  $\delta = 0$  in the sense explained in Fig. 5, so that different crack densities imply different vertical distances  $h$  and the  $\delta = 0$  positions are slightly shifted one with respect to the others (although the difference is not so evident on the graphic scale of Fig. 6).

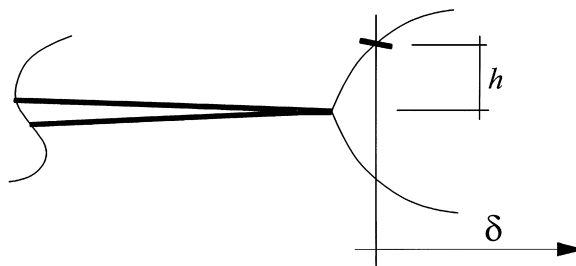


Fig. 5. Position of the first microcrack with respect to the main crack tip and to the limit of the saturated process zone.

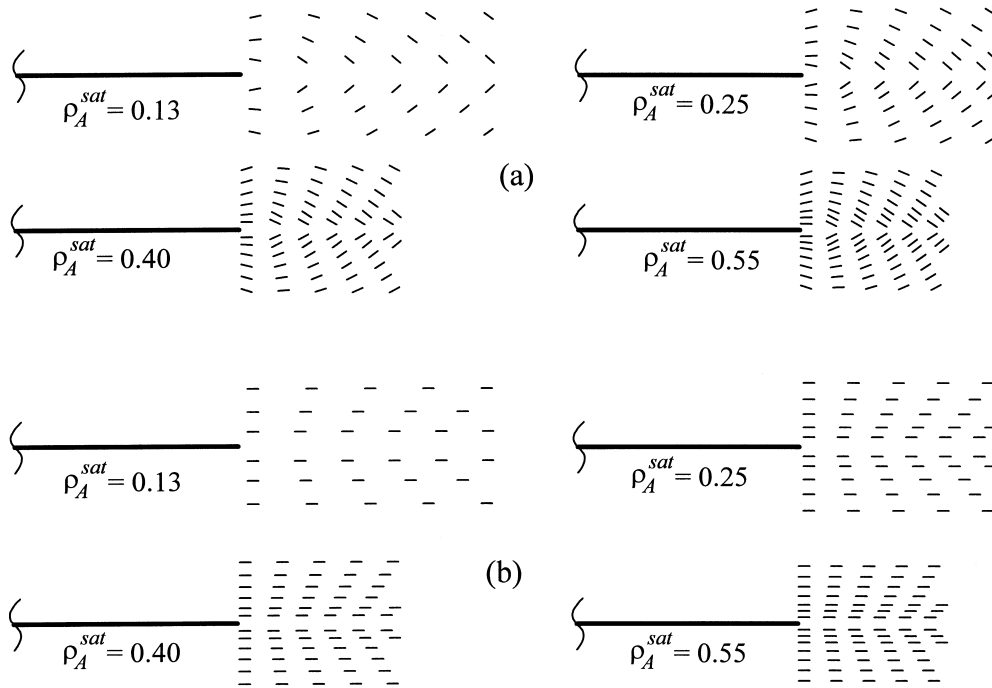


Fig. 6. Distributions of microcracks with different densities: (a) principal direction oriented cracks; (b) parallel cracks.

### 5. EFFECTS OF DAMAGE ON THE MAIN CRACK

The main crack and its process zone are thought of as located in an infinite plate made of linear hyper-elastic, homogeneous and isotropic material in plane strain state. At infinity, a uniform stress  $\sigma$  is applied so as to load the main crack in pure mode I; let the SIF induced at the main crack tip in absence of microcracks be  $K_{I0}$ . The position of the process zone relative to the main crack tip is identified by the parameter  $\delta$  as represented in Fig. 5.

For different values of the parameter  $\delta$ , the SIFs  $K_I$  and  $K_{II}$  at each tip had been calculated using a numerical procedure based on a displacement discontinuity boundary element formulation proposed by the authors[19], which proved to be efficient in fracture mechanics problems. It allows to take into account not only the interaction of the main crack with each microcrack, but also the mutual interactions between the microcracks. In this way, it is no longer necessary to postulate the hypothesis of *dilute limit* for non interacting microcracks, interactions which cannot be considered as negligible *a priori*.

Figure 7 plots the relative variation of the SIF at the main crack tip, which consists of  $K_I$  only for the symmetry of the problem, as a function of the position  $\delta$  of the macrocrack relative to the process zone for different saturation densities of the microcracks. The bold diagrams refer to the principal stress orientation, while thin ones are related to the process zone with microcracks parallel to the main crack.

The parts of the diagrams below the abscissae axis represent a relative decrease of the SIF at the main crack tip or, in other words, a *shielding* effect on the main crack, while the parts of the diagrams above the axis point out that, for some geometries, the stress field at the main crack tip turns out to experiment *amplifying* effects. It can be seen that the microcrack density does not affect the essential features of the interactive phenomena since it plays the role of a scaling coefficient which alters only the numerical values.

For  $\delta$  set in the range [0.5–1.5] according to the microcrack density, a strong shielding effect is experienced by the macroscopic crack, which is as strong as up to 40% of the reference value independently of the crack orientation. If we assume that the main crack propagation starts when the SIF at its tip equals the material fracture toughness  $K_{IC}$ , these specific positions account for some 11, 25, 33 and 66% increase of the load level which leads to propagation,

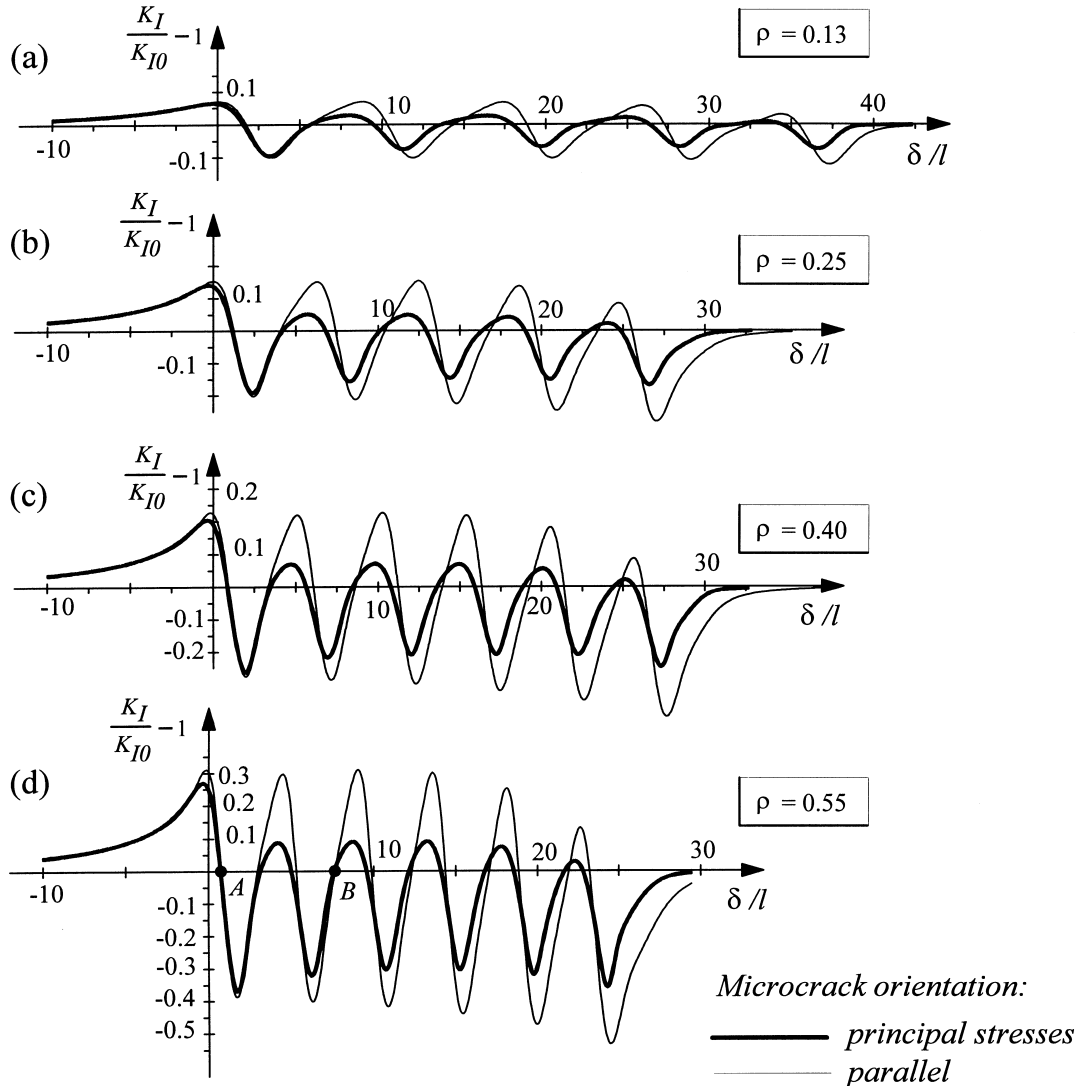


Fig. 7. Relative variation of the SIF at the main crack tip as a function of the saturated density and relative position  $\delta$ .

according to the microcrack saturated density. This estimate is affected by the simplicity of the model since the effects of a statistical distribution of microcracks as well as of macrocrack kinking are not included, but nevertheless quantifies the net contribution due to crack interaction mechanisms.

The same conclusion holds also on the average. Considering the first two complete waves of the diagrams [point A to B in Fig. 7(d)], the average effect is that of shielding the main crack some 5% of the reference value for parallel cracks and 21% for oriented cracks; This results is coherent with those obtained by Ortiz and Giannakopoulos[40] from a continuum model, which indicate that the microcracks oriented normal to the maximum tensile stress direction are the most efficient in shielding problems.

In addition, process zones simulated by parallel cracks induce stronger amplification and shielding effects than the microcracks oriented along the principal stress directions. Figure 7(c), for example, shows that parallel cracks amplify the main crack tip stress field three times more than the principal direction oriented cracks, while the shielding effects are only 15% stronger than those induced by oriented cracks.

Whatever the orientation is, the position  $\delta = 0$  of the microcracks is the one which experiences the strongest amplification, up to 30% of the reference value  $K_{I0}$  for strongly interacting

cracks ( $\rho = 0.55$ ). It is only the series of relative maxima after the first one that is greatly affected by microcrack orientation: parallel cracks induce an almost unchanged amplification, while the oriented cracks are able to induce an overall amplifying effect which is one third or less than the first maximum.

The last parts of the diagrams, for  $\delta/l > 25$ , represent geometries where the process zone is in large part or completely positioned in the wake zone. These microcrack settlements do not represent any physical situation because, when the stationary process zone has entered the wake area, a new and larger process zone should have already been nucleated in front of the main crack. Nevertheless, these geometries are meaningful because they make evident the net effect of the wake.

For large values of  $\delta/l$ , the main crack tip stress field rapidly approaches the abscissae axis: in other words, the effects of crack interaction disappear. While entering the wake area, the microcrack stress field vanishes too, so that open cracks gradually close and the hypothesis of a frictionless material allows previous sliding to be completely recovered.

## 6. ELASTIC STRAIN ENERGY

When a crack, contained in an elastic plate, is loaded in mixed mode conditions the elastic strain energy density related to the singular stress field at its tip can be expressed as a function of the SIFs  $K_I$  and  $K_{II}$  [23, 24] as:

$$\frac{dW}{dV} = \left[ a_{11} \frac{K_I^2}{\pi} + 2a_{12} \frac{K_I K_{II}}{\pi} + a_{22} \frac{K_{II}^2}{\pi} \right] \frac{1}{r} = \frac{S(\theta)}{r}, \quad (22)$$

where

$$a_{11} = \frac{1}{16G} (1 + \cos \theta)(\kappa - \cos \theta), \quad (23a)$$

$$a_{12} = \frac{1}{16G} \sin \theta [2 \cos \theta - (\kappa - 1)], \quad (23b)$$

$$a_{22} = \frac{1}{16G} (1 - \cos \theta)(\kappa + 1), \quad (23c)$$

and constant  $\kappa$  stands for:

$$\kappa = 3 - 4\nu \quad (23d)$$

for plane strain and:

$$\kappa = \frac{3 - \nu}{1 + \nu} \quad (23e)$$

for plane stress.

The contribution of the singular stress field to the global elastic strain energy relative to a single crack can be obtained by integrating eq. (22) over a circular area of radius  $R^*$  centred in the crack tip, which leads, for a unitary thickness, to the following expression:

$$W_{R^*} = \frac{1}{16G} [K_I^2(2\kappa - 1) + K_{II}^2(2\kappa + 3)] \int_0^{R^*} dr = W_{R^*}^I + W_{R^*}^{II}. \quad (24)$$

Equation (24) points out that the strain energy absorbed by a crack consists of two separate terms, each one referred to an elementary loading mode and without the term containing both the SIFs: the strain energy related to a crack is decoupled with regard to the loading mode. The quantity  $W_{R^*}$  in eq. (24) turns out to be very similar to the classical energy release rate  $\mathcal{G}$ .

Since this result has been obtained integrating eq. (24) only over the angle  $\theta$ , the radius  $R^*$  has to be defined. In mixed mode conditions  $K_I$  and  $K_{II}$  are in general different and the symmetric and antisymmetric stress fields contribute by different amounts to the global strain energy

of the solid: the integration in eq. (24) has thus to be carried out over different radii  $R^*$  for the two loading modes.

It is a reasonable hypothesis that the contribution to the elastic strain energy is negligible when the tangent to the stress function is lower than a fixed value  $\alpha$ :

$$\left(\frac{\partial \sigma_r}{\partial r}\right)_{R^*} = \alpha \quad \text{and} \quad \left(\frac{\partial \tau_{r\theta}}{\partial r}\right)_{R^*} = \alpha, \tag{25a, b}$$

which lead to the following definitions:

$$R_I^* = \sqrt[3]{\frac{1}{8\pi} \left(\frac{K_I}{\alpha}\right)^2}, \tag{26a}$$

for symmetric loading and:

$$R_{II}^* = \sqrt[3]{\frac{1}{8\pi} \left(\frac{K_{II}}{\alpha}\right)^2}, \tag{26.b}$$

for antisymmetric loading.

The elastic strain energy related to a single crack tip is therefore expressed by the following equation:

$$W_{R^*} = \frac{1+\nu}{8E} \left[ K_I^2 (2\kappa - 1) \sqrt[3]{\frac{1}{8\pi} \left(\frac{K_I}{\alpha}\right)^2} + K_{II}^2 (2\kappa + 3) \sqrt[3]{\frac{1}{8\pi} \left(\frac{K_{II}}{\alpha}\right)^2} \right]. \tag{27}$$

The value  $\alpha = 0.01$  represents the limit for which the asymptotic stress field differs from its asymptote for not more than 1% and Fig. 8 represents the connection between the tangent and the radius  $R^*$  established by the previous equations.

### 7. STRAIN ENERGY RELATED TO THE MAIN CRACK AND THE MICROCRACKS

The numerical technique used to investigate the interactive effects allows the computation of the SIFs at each microcrack tip as well as at the main crack one. Being the bi-dimensional domain infinite and loaded at infinity with a uniform static load, no influence and dissipation is to be expected from the finite boundaries, so that the total strain energy related to the process zone is obtained summing up the contributions  $W_{R^*}^{mc}$  like eq. (24) of each microcrack tip and the global strain energy  $W_{R^*}^T$  is then obtained adding the contribution  $W_{R^*}^{MC}$  due to the main crack:

$$W_{R^*}^T = W_{R^*}^{MC} + \sum_{mc=1}^{n_{mc}} W_{R^*}^{mc}, \tag{28}$$

where  $n_{mc}$  represents the total number of microcracks.

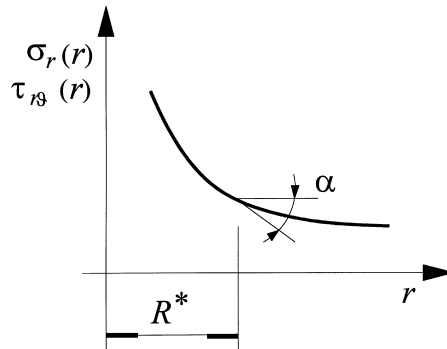


Fig. 8. Relationship between the tangent to the stress function and the radius  $R^*$ .

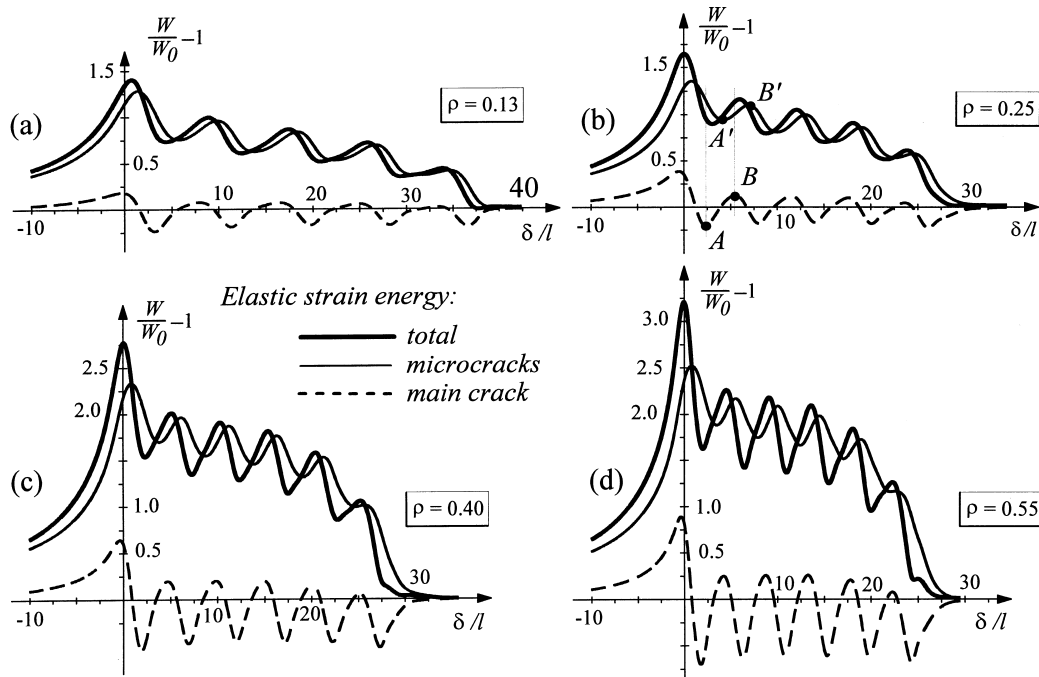


Fig. 9. Strain energy variation as a function of the relative position  $\delta$  (all microcracks oriented as the principal directions).

Figure 9 represents the relative variation of strain energy as a function of the position  $\delta$  between the main crack and the process zone for different microcrack densities all oriented like the principal directions. Bold lines stand for the total strain energy, while thin diagrams show the energy rate due only to the process zone microcracks. Finally, dashed lines represent the strain energy related to the main crack. The normalizing quantity  $W_0$  is the strain energy due to the main crack under the same loading conditions and without microcracks.

The maximum energy content is related to the position  $\delta = 0$ , while, when the main crack enters the process zone, the total elastic strain energy decreases and turns out to be not constant and a non monotonically decreasing function of  $\delta$  on the average. The total energy content is mainly due to the microcracks, the main crack being responsible for some 17–20% of the global strain energy; the main crack energy contribution resembles the  $K_I$  function,  $K_{II}$  being zero for symmetry. The points in which the dashed diagram intersects the abscissae axis are called *neutral points* in the sense that the main crack does not feel the interaction with the process zone, i.e. the microcrack effects are globally zero.

The diagram of energy content in the process zone—thin lines, points A' and B'—is slightly shifted with respect to the main crack one, points A and B in Fig. 9(b), so that the relative extremes, maxima and minima of the microcrack energy content, correspond alternately to the main crack neutral points. Therefore, it can be said that the minimum energy content related to the microcracks does not correspond to the maximum microcrack shielding, but to a condition in which the effect of the microcracks is globally equal to zero.

Figure 10 represents the analogous diagrams for microcracks all parallel to the main crack; the trends in strain energy variations are similar to those discussed in the previous section. Only one difference emerges: in the  $\delta = 0$  position, the total energy is not maximum; in fact, the maximum strain energy is obtained for the main crack deeply inside the process zone. The total energy is not, in this case, a non-monotonically decreasing function on the average.

A comparison between the global strain energy content for the same saturated microcrack densities, but for different crack orientations is represented in Fig. 11. The bold lines are referred to the microcracks oriented perpendicular to the principal tensile direction, while the thin lines had been obtained for parallel cracks. An outstanding remark is straightforward: parallel cracks are associated to a global elastic strain energy content which is always higher than

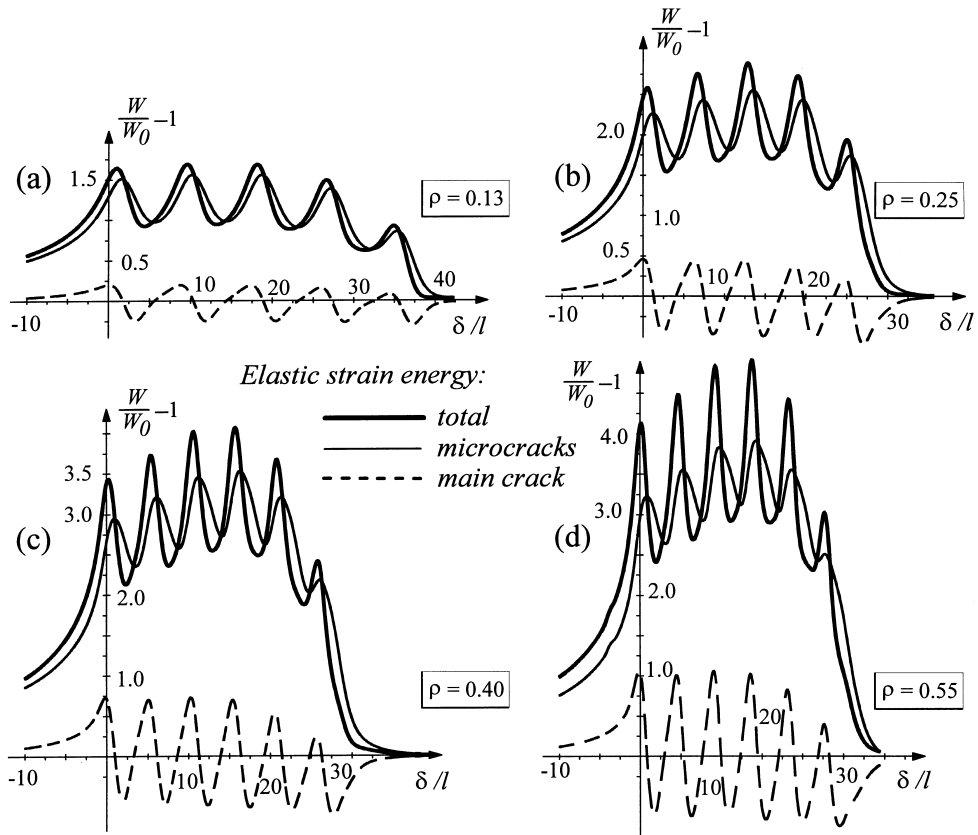


Fig. 10. Strain energy variation as a function of the relative position  $\delta$  (all microcracks parallel to the main crack)

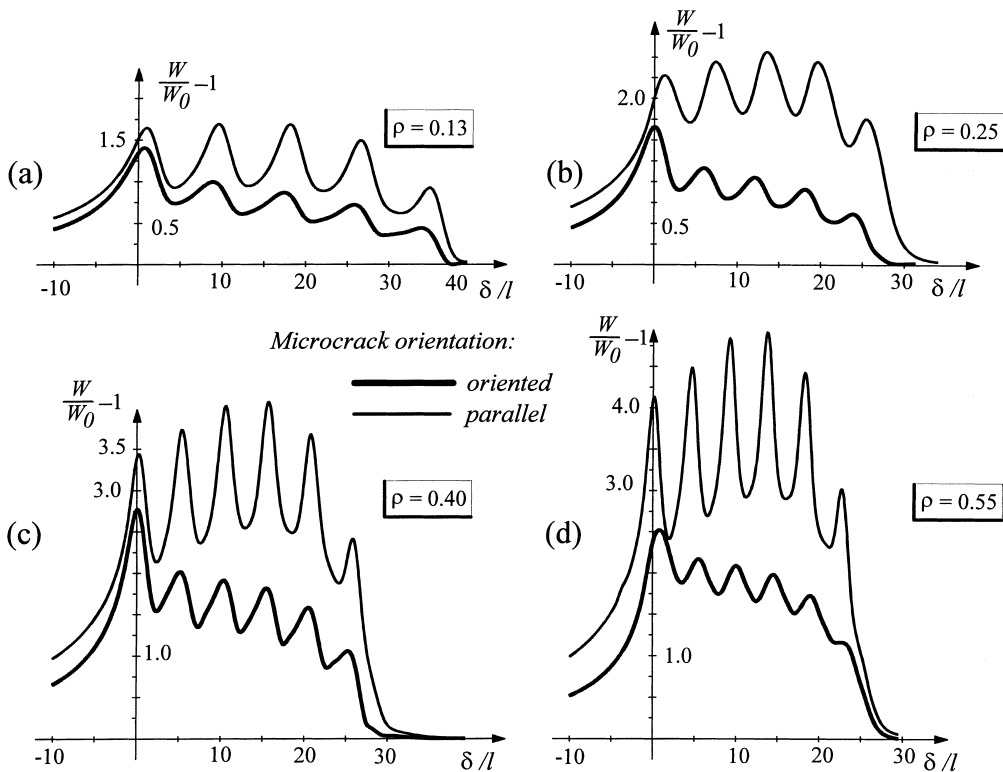


Fig. 11. Strain energy variation for parallel and oriented cracks at different saturated densities.

the energy related to oriented microcracks; for the highest densities, it is twice the energy absorbed by oriented cracks.

## 8. ELASTIC STRAIN ENERGY DISTRIBUTION INSIDE THE PROCESS ZONE

In previous sections, the extension of the microcrack distribution that can constitute an acceptable model for the stationary frontal process zone has been discussed. In this section, the elastic strain energy distribution inside the microcrack settlement is analysed, giving further reasons for considering the approximations introduced into the model.

Let us define  $\Delta$  as the extension of the process zone in the direction of the main crack axis, which is approximately 1.5 times the estimate  $R_{\text{sat}}$  given in eq. (14b) according to the results obtained by Hoagland and Embury [36] discussed in Section 4. Five circular regions, with increasing radius and centred on the macrocrack tip, can be distinguished inside the microcrack distribution, Fig. 12.

Some microcrack tips are found inside each area, so that the elastic strain energy related to each zone can be computed according to eq. (27). Figures 13 and 14 show five different diagrams for each saturated density, the lower diagram being the elastic strain energy inside the first circular region, while the upper diagrams are related to the other areas with increasing radius. Both orientations, perpendicular to the maximum tensile stress direction and parallel to the main crack, are considered.

As far as the radius increases, the elastic strain energy content increases too, but with a non-linear dependence upon the radius  $R^*$ . Although the maximum contribution to the total energy is due to the cracks contained in the inner zone, nevertheless the outer areas give a relevant and not negligible contribution.

The positions of the main crack relative to the microcrack distribution that can be considered physically meaningful are those identified by the values of the non-dimensional parameter  $\delta/l$  in the range [0.5–10]. These geometric settlements correspond to the onset of macrocrack propagation before new microcracks are nucleated and before a transient regime, from stationary to steady growing conditions, is established. Inside these limits, for all microcrack densities and both the orientations analysed, it can be found that the inner area 1 is responsible for the 60% of the total strain energy in the process zone, as well as the outer regions 2, 3, 4 and 5 contribute, respectively, to the total microcrack energy for the 18, 11, 7 and 4% on the average.

The straightforward conclusions are that the aforementioned approximations about the interaction range set in eq. (19) are valid (also cracks in region 5 give moderate contribution to the global elastic strain energy content) and, at the same time, the interacting microcracks which are more distant from the macrocrack tip than usually supposed need to be considered for a satisfactory simulation of the process zone (contribution from areas 2, 3 and 4).

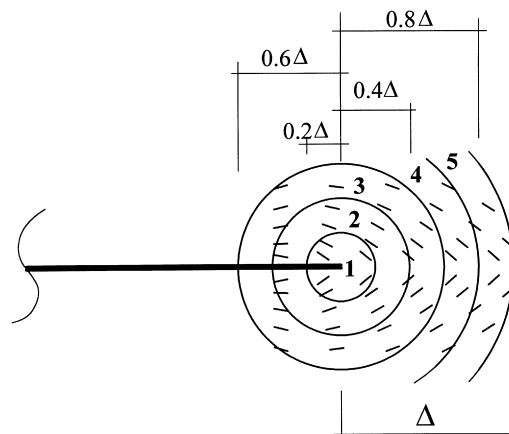


Fig. 12. Five different areas around the main crack tip.

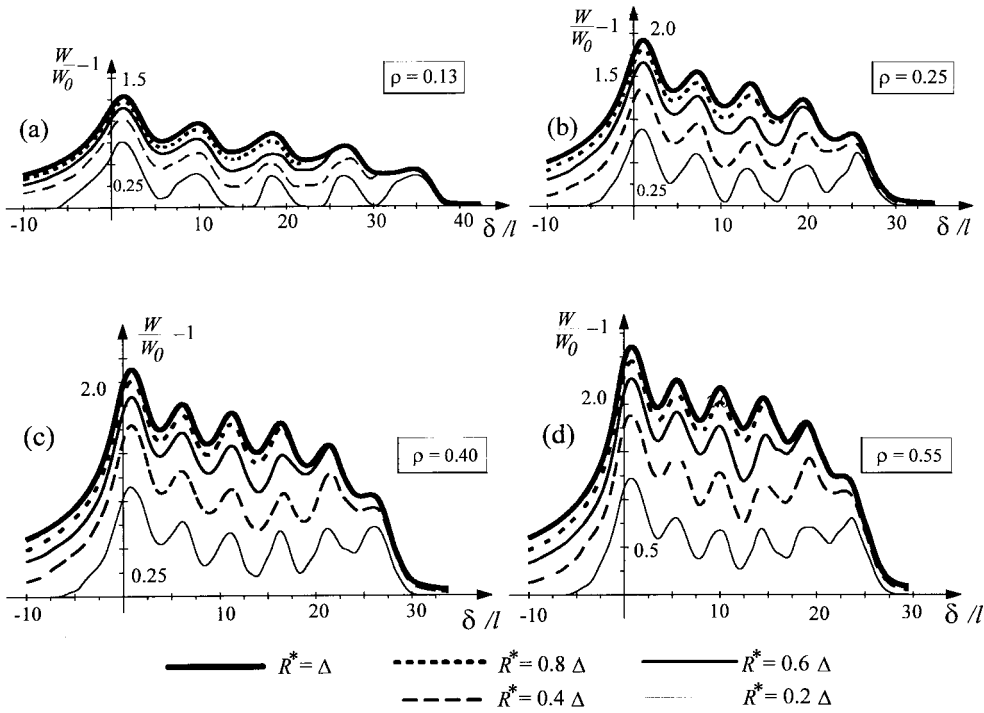


Fig. 13. Energy distribution inside the process zone as a function of the radius  $R^*$  and the distance  $\delta$  (oriented microcracks).

If less detailed information is needed, the extension of the microcracked area can be limited more severely than what is shown in eq. (19). Neglecting the microcracks located in areas 5 and 4 only the saturated part of the microcracked area can be considered, in the same way as in Ref.[36].

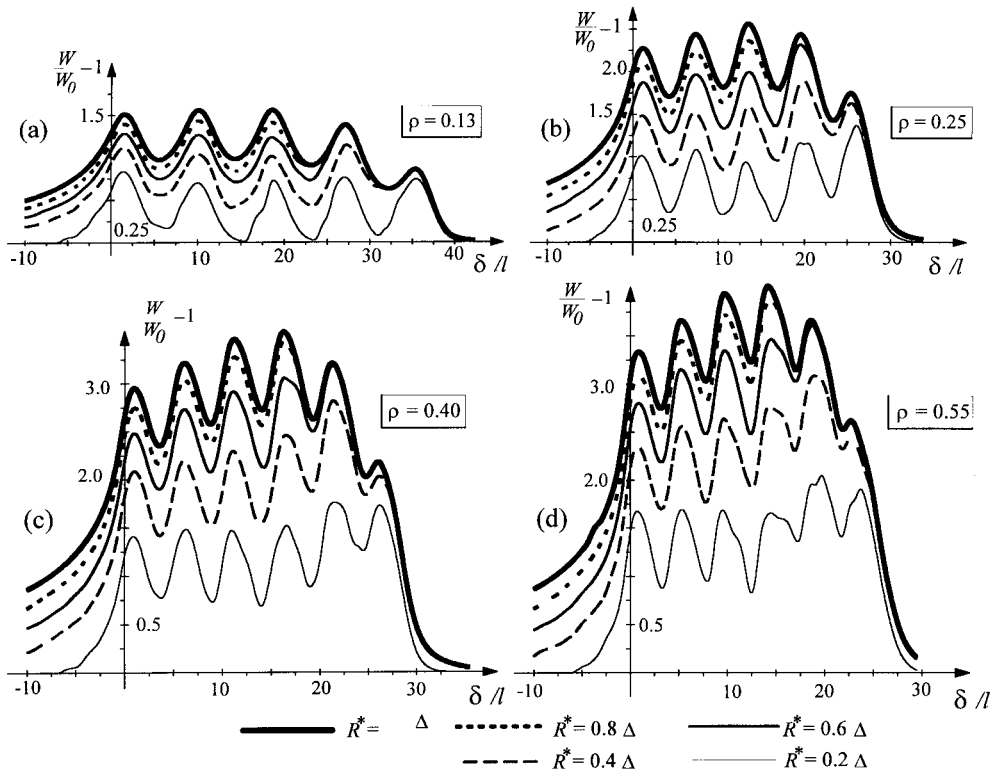


Fig. 14. Energy distribution inside the process zone as a function of the radius  $R^*$  and the distance  $\delta$  (parallel microcracks).

In addition, focusing the attention on the stress fields, it is found that all the microcracks experience mixed mode loading with a prevailing mode I component. In area 1 the cracks closest to the main crack tip exhibit a  $K_I$  value that never exceeds 20–25% of the main crack  $K_I$ . In the outer region 5, the microcrack SIFs range from zero to about 4–5% of the main crack SIF in mode I. In the whole process zone the  $K_{II}$  values remain about 25% of the  $K_I$  value at the same tip.

At the end of Section 5, it has been pointed out that microcracks located in the wake zone do not give rise to any interaction with the main crack tip. Figures 13 and 14 confirm the same results, showing that when cracks are completely located in the wake (large values for  $\delta/l$ ) the elastic strain energy associated to the microcrack system equals zero; in these conditions, the global energy content is due only to the macroscopic cracks. These conclusions are to be intended as the net effect of the wake, as previously explained.

## 9. DISCUSSION AND CONCLUSION

Experimental evidence brought attention to the interaction mechanisms which are established when a microcracked process zone develops in front of a macrocrack. Two essential features of the damaged area are outstanding: (1) the microcrack orientation is perpendicular to the principal tractions, but for some small variations due to microstructural inhomogeneity; and (2) the process zone is rather long in front of the main crack tip.

Based on the concept of *crack precursor* introduced by Hoagland and Embury [36] and Gong [22], a simulation of the microcrack distribution for a stationary crack has been proposed in which the microcrack density lowers as the distance from the main crack is increased. An essential feature of the model is that the definition of microcrack length is connected to some material properties (the tensile strength  $\sigma_n^{\text{lim}}$  and the toughness  $K_{IC}$  of the material), rather than to some semi-empirical criteria.

The analysis of interactive effects of the process zone on the main crack pointed out that the principal traction orientation of the microcracks is responsible of an average shielding of the macrocrack much more pronounced than that induced by parallel cracks. The microcrack saturated density does not affect the essential features of the phenomenon, being only responsible for an increase in the numerical values.

Through integration, it has been shown that the superposition principle holds also for the elastic strain energy associated to the singular stress field at each crack tip. The evaluation of the total strain energy related to the main crack-process zone system pointed out that when the microcracks are oriented the strain energy content is lower than the energy for parallel cracks, giving a tool for understanding why microcracks nucleate very close to the principal directions.

The analysis of the energy distribution inside the damaged material, as long as a similar investigation on the microcracks, confirmed that the interaction range is quite larger than sometimes supposed, as already discussed in Ref. [19]. In particular the outer part of the microcrack distribution is responsible of approximately 40% of the whole energy content.

The results, obtained for an infinite linear elastic plate, give evidence to an important and not trivial remark. Considering the main crack and the microcracks as a whole, the energy absorbed by this system is not constant as the position  $\delta$  between the microcrack cloud and the main crack tip is changed. These results, altogether, give some explanations on the shape and extension of the experimentally observed process zones.

*Acknowledgements*—The authors gratefully acknowledge the financial support of the National Research Council (CNR), the Department for University and Scientific and Technological Research (MURST) and the EC-TMR Contract No. ERBFMRXCT960062.

## REFERENCES

1. Hoagland, R. G., Embury, J. D. and Green, D. J., On the density of microcracks formed during the fracture of ceramics. *Scripta Metall.*, 1973, **9**, 907–909.
2. Han, L. X. and Suresh, S., High-temperature failure of an alumina–silicon carbide composite under cyclic loads: mechanisms of fatigue crack tip damage. *J. Am. Ceram. Soc.*, 1989, **72**, 1233–1238.
3. Rühle, M., Evans, A. G., McMeeking, R. M., Charalambides, P. G. and Hutchinson, J. W., Microcrack toughening in alumina/zirconia. *Acta Metall.*, 1987, **35**, 2701–2710.

3. Rühle, M., Evans, A. G., McMeeking, R. M., Charalambides, P. G. and Hutchinson, J. W., Microcrack toughening in alumina/zirconia. *Acta Metall.*, 1987, **35**, 2701–2710.
4. Rühle, M., Claussen, N. and Heuer, A. H., Transformation and microcrack toughening as complementary processes in ZrO<sub>2</sub>-toughened Al<sub>2</sub>O<sub>3</sub>. *J. Am. Ceram. Soc.*, 1986, **69**, 605–797.
5. Kreher, W. and Pompe, W., Increased fracture toughness of ceramics by energy-dissipative mechanisms. *J. Mater. Sci.*, 1981, **16**, 694–706.
6. Dolgopolsky, A., Karbhari, V. and Kwak, S. S., Microcrack induced toughening—an interaction model. *Acta Metall.*, 1989, **37**, 1349–1354.
7. Fu, Y. and Evans, A. G., Some effects of microcracks on the mechanical properties of brittle solids. I. Stress, strain relations; and II. Microcrack toughening. *Acta Metall.*, 1985, **33**, 1515–1531.
8. Hutchinson, J. W., Crack tip shielding by micro-cracking in brittle solids. *Acta Metall.*, 1987, **35**, 1609–1619.
9. Ortiz, M., A continuum theory of crack shielding in ceramics. *J. Appl. Mech.*, 1987, **54**, 54–58.
10. Charalambides, P. G. and McMeeking, R. M., Finite element method simulation of crack propagation in a brittle microcracking solid. *Mech. Mater.*, 1987, **6**, 71–87.
11. Alpa, G. and Gambarotta, L., The elastic crack interaction in modelling materials. *Eng. Fract. Mech.*, 1993, **46**, 663–676.
12. Kachanov, M., Montagut, E. L. and Laures, J. P., Mechanics of crack–microcrack interactions. *Mech. Mater.*, 1990, **10**, 59–71.
13. Horii, H. and Nemat-Nasser, S., Elastic fields of interacting inhomogeneities. *Int. J. Solids Struct.*, 1985, **21**, 731–745.
14. Rubinstein, A. A., Macrocrack interaction with semi-infinite microcrack array. *Int. J. Fracture*, 1985, **27**, 113–119.
15. Rose, L. R., Microcrack interaction with a main crack. *Int. J. Fracture*, 1986, **31**, 233–242.
16. Kachanov, M., Elastic solids with many cracks: a simple method of analysis. *Int. J. Solids Struct.*, 1987, **23**, 23–43.
17. Rubinstein, A. A. and Choi, H. C., Macrocrack interaction with transverse array of microcracks. *Int. J. Fracture*, 1988, **36**, 15–26.
18. Gong, S. X. and Horii, H., General solution to the problem of microcracks near the tip of a main crack. *J. Mech. Phys. Solids*, 1989, **37**, 27–46.
19. Brencich, A. and Carpinteri, A., Interaction of a main crack with ordered distributions of microcracks: a numerical technique by displacement discontinuity boundary elements. *Int. J. Fracture*, 1996, **76**, 373–389.
20. Huang, X. and Karihaloo, B. L., Interaction of penny shaped cracks with a half plane crack. *Int. J. Solids Struct.*, 1993, **25**, 591–607.
21. Portela, A., Aliabadi, M. H. and Rooke, D. P., Dual boundary element incremental analysis of crack propagation. *Comput. Struct.*, 1993, **46**, 237–247.
22. Gong, S. X., On the formation of near-tip microcracking and associated toughening effects. *Engng Fracture Mech.*, 1995, **50**, 29–39.
23. Sih, G. C., Some basic problems in fracture mechanics and new concepts. *Engng Fracture Mech.*, 1973, **5**, 365–377.
24. Sih, G. C., Strain-energy-density factor applied to mixed mode crack problems. *Int. J. Fracture*, 1974, **10**, 305–321.
25. Shum, K. M. and Hutchinson, J. W., On toughening by microcracks. *Mech. Mater.*, 1990, **9**, 83–91.
26. Bristow, J. R., Microcracks and the static and dynamic elastic constants of annealed and heavily cold-worked metals. *Brit. J. Appl. Phys.*, 1960, **11**, 81–95.
27. Walsh, J. B., The effect of cracks on the compressibility of rocks. *J. Geophys. Res.*, 1965, **70**, 381–389.
28. Walsh, J. B., The effect of cracks on uniaxial compression of rocks. *J. Geophys. Res.*, 1965, **70**, 399–411.
29. Kachanov, M., Elastic solids with many cracks and related problems. *Adv. Appl. Mech.*, 1993, **30**, 259–445.
30. Budiansky, B. and O'Connell, R. J., Elastic moduli of a cracked solid. *Int. J. Solids Struct.*, 1976, **12**, 81–97.
31. Underwood, E. E., *Quantitative stereology*. Addison Wesley, NJ, 1968.
32. Hadley, K., Comparison of calculated and observed crack densities and seismic velocities in Westerly granite. *J. Geophys. Res.*, 1976, **81**, 3484–3494.
33. Gawad, M. A., Bulan, J. and Tittmann, B., Quantitative characterization of microcracks at elevated pressures. *J. Geophys. Res.*, 1987, **92**(12), 911–12916.
34. Nemati, K. M., Generation and interaction of compressive stress-induced microcracks in concrete. PhD Thesis, Department of Civil Engineering, University of California at Berkeley, 1994.
35. Nemati, K. M. and Monteiro, P. J. M., Effect of confinement on the fracture behaviour of concrete under compression. In *Fracture Mechanics of Concrete Structures: Proceedings of FRAMCOS-2, Second International Conference on Fracture Mechanics of Concrete and Concrete Structures*, vol III, ed. F. H. Wittmann. Aedificatio, Freiburg, 1996, pp. 1843–1852.
36. Hoagland, R. G. and Embury, J. D., A treatment of the inelastic deformation around a crack tip due to microcracking. *J. Am. Ceram. Soc.*, 1980, **63**, 404–410.
37. Gong, S. X. and Meguid, S. A., On the effect of the release of residual stresses due to near-tip microcracking. *Int. J. Fracture*, 1991, **52**, 257–274.
38. Brencich, A. and Carpinteri, A., Interaction of a main crack with ordered distributions of microcracks. In *Fracture Mechanics of Concrete Structures: Proceedings of FRAMCOS-2, Second International Conference on Fracture Mechanics of Concrete and Concrete Structures*, vol 1., ed. F. H. Wittmann. Aedificatio, Freiburg, 1995, pp. 363–372.
39. Kachanov, M., and Montagut, E. L. Interaction of a crack with certain microcrack arrays. *Engng Fracture Mech.*, 1985, **25**, 625–636.
40. Ortiz, M. and Giannakopoulos, A. E., Maximal crack tip shielding by microcracking. *J. Appl. Mech. (ASME)*, 1989, **56**, 279–283.